

Nanofriction and motion of topological defects in self-organized ion Coulomb crystals

J. Kiethe¹, R. Nigmatullin², T. Schmirander¹, D. Kalincev¹, T.E. Mehlstäubler¹

¹ Physikalisch-Technische Bundesanstalt, Bundesallee 100, 38116 Braunschweig, Germany

² Complex Systems Research Group, Faculty of Engineering and IT, The University of Sydney, Sydney, New South Wales 2006, Australia

E-mail: tanja.mehlstaebler@ptb.de

Abstract. We study nanofriction in an ion Coulomb crystal under the presence of topological defects. We observe signatures of the pinning to sliding transition, namely the transverse vibrational soft mode signaling the transition and the symmetry breaking of the crystal configuration. We present details on experimental measurements and numerical simulations of this system, including the gaps in the hull function and the spectroscopy of the localized defect mode. We also investigate how external forces, such as those due to anharmonic potentials or differential light pressure, break the intrinsic crystal symmetry, thereby reducing mode softening near the sliding transition. We find that the local structure and position of the topological defect is essential for the presence of the soft mode and illustrate how the defect changes its properties, when it moves through the crystal.

PACS numbers: 37.10.Ty, 05.70.Fh, 02.70.Ns

Keywords: *nanofriction, topological defects, trapped ions, Coulomb crystals, discrete solitons*

1. Introduction

Friction influences many natural phenomena over several orders of magnitude of relevant length scales, from earthquakes to biological molecules [1]. Especially nanofriction processes on the atomic scale are nowadays of technical importance, due to advances made in such fields as nanofabrication [2] and biotechnology [3, 4]. To gain insights into the *in-situ* dynamics of nanofriction processes, an emulation via laser-cooled and trapped ions was proposed [5–9]. These works suggested emulating one of the most fundamental models of nanofriction, i.e. the Frenkel-Kontorova (FK) model [10], using ion chains in an optical lattice [11–13]. Following the proposals, Bylinskii *et al.* were able to trap 5 ions in an optical lattice, demonstrating the onset of reduced friction [14], the velocity dependence of the stick-slip motion [15], as well as single ion multi-slip behavior [16]. Furthermore, they observed structural symmetry-breaking at the pinning to sliding transition [17], an Aubry-type (AT) transition.

In actual nanocontacts, two layers of atoms are interacting with each other. The corrugation is then no longer given by a rigid potential, but rather by a deformable layer [18]. Recently, we presented a self-organized system, consisting of two deformable back-acting ion chains, without a fixed corrugation potential [19]. We showed, that two-dimensional ion Coulomb systems under the presence of a topological defect [20–23] exhibit features of an Aubry-type transition, namely the breaking of analyticity of a hull function and a soft phonon mode. We also observed the symmetry breaking inside the crystal, which is a typical signature of finite systems [12, 13]. Our system shows similarities to other self-organized sliding systems, such as fibrous composite materials [4], sliding DNA strands [24] and propagation of protein loops [25]. While the investigation of nanofriction with the help of discrete topological defects, also known as kink solitons, is a new approach, these defects have been extensively studied with respect to the Kibble-Zurek mechanism [20–23, 26–28] and to quantum information [29, 30]. Also, the directed transport of topological defects via a ratchet mechanism has been recently reported [31].

In the following we discuss in more detail our experimental and numerical findings of this tribological system. We explain our approach to the calculation of the hull function in self-organized systems and

discuss secondary gaps in the hull functions due to the inhomogeneity of the charge density. We detail our spectroscopic method, which was used to probe the localized kink soliton mode, transition from sticking to sliding. We also study the influence of temperature on the vibrational spectra using molecular dynamics simulations and Fourier transformation techniques. We numerically investigate external forces that break the local crystal symmetry, and influence the mode frequencies of the system. Forces under investigation result from effects, such as anharmonicities of the axial trapping potential, axial micromotion and laser light pressure. We show, that the position of the topological defect is sensitive to forces on the 10^{-21} N level. We numerically investigate the motion of extended topological defects through the crystal induced by differential light forces, and discuss the associated periodic change in their physical properties, such as local structure and mode frequency.

This paper is structured in the following way. Section 2 introduces our experimental system and describes the observation of two main features of the Aubry-type transition in finite atomic systems, namely the symmetry breaking and the soft vibrational mode. Then we introduce the definitions of an order parameter and the hull functions, and how they can be applied to self-organized systems. In Section 3 we analyze external forces that could break the intrinsic crystal symmetry. Building on these results, in Section 4, we study the behavior of the topological defect, as it is moved through the crystal. Finally, in Section 5, we discuss our results and give an outlook to future experiments and theoretical investigations.

2. Pinning to sliding transition in a self-organized system

Our system consists of a two-dimensional ion Coulomb crystal in the zigzag phase with an extended topological defect in the center. The frictional process of interest is the sliding of the two chains against each other. In the following, we focus on the axial vector components of the motion, reducing the system to a one-dimensional problem. The interaction energies within the chains, U_{intra} , and between the chains, U_{inter} , characterize the regime of friction. To determine the critical point, we can estimate these energies from the characteristic distances in the Coulomb crystals. To do so, we model the

two linear chains as classical particles of mass m , which interact within each chain via springs with constant κ_i , where i is 1 or 2, identifying the chains as illustrated in Figure 1(a). The spring constants of the chains are different, due to the topological defect introducing a small mismatch between the interion distances a_i . The chains are separated by a distance b and all masses are connected to a rigid support by springs of stiffness $D = m\omega_z^2$, which corresponds to the axial confinement of the ion trap ω_z . Moving the chains against each other can be done via light forces acting on each chain independently, which we name F_i . Given this simplified model we can employ a harmonic approximation to roughly estimate the interaction energy of ions within the top chain as $U_{\text{intra}} \approx \frac{1}{2}\kappa_1 z^2$. The energy scale of the corrugation by the other chain can locally be approximated as $U_{\text{inter}} \approx \frac{1}{2}U_0 [\cos(2\pi a_2^{-1}z) + 1]$, where U_0 is the strength of the corrugation, which depends on b . If the chains are brought closer together U_0 increases, changing the relative strength of the interactions. At a certain distance a critical depth of the corrugation potential U_c is crossed and the system changes from the sliding to pinning regime. At this point we expect a symmetry breaking of the crystal structure as illustrated in Figure 1(b).

The transition should happen when the competing energies are in balance. Representing these energies as angular frequencies in the harmonic approximation:

$$\omega_{\text{pinning}} = \sqrt{2\pi^2 U_0 (ma_2^2)^{-1}} \quad \text{and} \quad \omega_{\text{natural}} = \sqrt{\kappa_1 m^{-1}}$$

we can define a dimensionless corrugation parameter

$$\eta = \frac{\omega_{\text{pinning}}^2}{\omega_{\text{natural}}^2}. \quad (1)$$

At the transition we therefore expect an η of order 1.

In order to estimate η , we approximate the frequencies ω_{pinning} and ω_{natural} , which describe a many-body interaction, with the help of the potentials, seen by one of the central ions. In a two-dimensional Coulomb crystal with a topological defect shown in Figure 1(b), both central ions are located on the slope of U_{inter} . As a harmonic approximation is not valid there, we use the interaction energies \tilde{U}_{inter} and \tilde{U}_{intra} of a zigzag without defect as a further approximation. In such a crystal, all ions of one chain are located in the potential minimum of \tilde{U}_{inter} . The second-order Taylor expansion of \tilde{U}_{inter} and \tilde{U}_{intra} are then proportional to the approximate frequencies $\tilde{\omega}_{\text{pinning}}$ and $\tilde{\omega}_{\text{natural}}$, respectively. This will result in an approximate corrugation parameter $\tilde{\eta}$, which has a critical value $\tilde{\eta}_c$ different from 1.

2.1. Experimental system

In this section we detail the experimental parameters necessary for implementing the above model system.

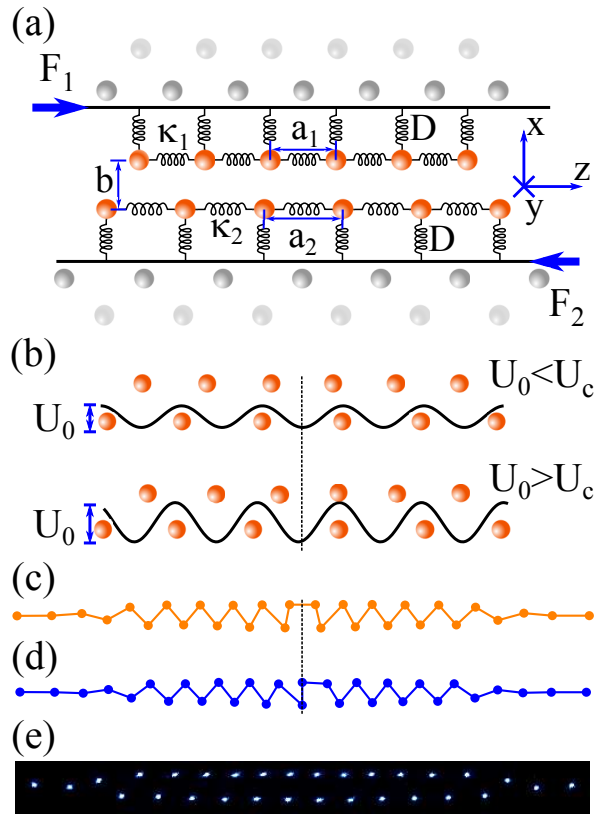


Figure 1. Nanofriction model system in a self-organized ion Coulomb crystal. (a) The central part of a Coulomb crystal can be seen as a back-acting interface between two atomically flat surfaces. Connection to a rigid solid (in our system the trap) is modeled with springs of strength D . Particles in one chain interact via springs of strength $\kappa_{1/2}$, which depend on the intra chain spacing $a_{1/2}$. The distances are not identical, due to the topological defect. The inter chain distance b determines the corrugation. Sliding of the model can be emulated by pushing one chain with force F_1 , and pushing the other with force F_2 . The coordinate system defines the axial (z) and radial (x) direction. (b) Symmetry breaking above the critical corrugation strength U_c . Decreasing the distance b between the chains, increases the corrugation until it crosses U_c and the defect moves away from the center (dashed line). (c) Horizontal kink. The two inner most ions are in the same chain. The number of ions in the upper and lower chain is different. The dashed chain shows the symmetry axis. (d) Vertical Kink. The two center ions are in different chains. The number of ions per chain is identical. (e) Experimental image of a horizontal defect. Exposure time is 700 ms. The xz plane of the crystal has an angle of approximately 40° to the CCD chip, resulting in a reduced observed radial distance between the chains. Graphics (a) and (b) are from [19].

We trap an ion Coulomb crystal with 30 $^{172}\text{Yb}^+$ ions in a high-precision linear Paul trap [32]. The ion trap chips are laser-machined with low tolerances and carefully aligned to reduce symmetry breaking of the electrode configuration. This reduces unwanted odd numbered anharmonic terms in the axial potential seen by the ions. The ions are laser-cooled on the strong $^2\text{S}_{1/2} \rightarrow ^2\text{P}_{1/2}$ dipole transition to temperatures in the low mK regime. The laser has a central wavelength of 369.5 nm and a beam diameter of 2.56 mm in axial (z) and 80 μm in radial ($\approx \sqrt{x^2 + y^2}$) direction. Typical laser powers are 200 μW to 300 μW . The fluorescence of the ions is imaged onto an electron multiplying (EM) 512×512 pixel CCD camera via a lens system with NA = 0.2 and magnification 24. The crystals xz plane has an angle of roughly 40° to the CCD chip. This reduces the observed radial distance between the ions. On the camera we can resolve individual ions and for an exposure time of 700 ms an ion position in a pure zigzag configuration can be resolved to 40 nm by fitting a Gaussian profile to the image. If the system is close to the Aubry-type transition, the resolution for the central ions, which are part of the topological defect, worsens.

In order to confine the crystal to the two-dimensional xz plane, we lift the degeneracy between the two radial potentials with the help of the dc potentials [32, 33], achieving a radial anisotropy of $\omega_x/\omega_y = 1.3$. In a two-dimensional crystal, the observed structural phase depends only on the relative magnitude of the transverse and axial confinement, quantified by the ratio of the respective secular frequencies $\alpha \equiv \omega_x/\omega_y$. This parameter is used in our calculations and experiments as a control to change the distance b and subsequently the corrugation η . For $4.81 < \alpha < 13.6$ a crystal with 30 ions will be in the two-dimensional zigzag phase [34].

For a fixed axial secular frequency $\omega_z \approx 2\pi \cdot 25$ kHz, topological defects can be created by rapidly quenching the rf amplitude of the radial confinement [21]. In terms of radial secular frequencies, this quench changes the confinement from $\omega_x \approx 2\pi \times 500$ kHz to values ranging from $2\pi \times 140$ kHz to $2\pi \times 200$ kHz in 58 μs . During this quench, several types of topological defects can be created in a finite ion Coulomb crystal in the two-dimensional phase [34]. The defect type is determined by the control parameter α . For an ion number $N = 30$ and the trap ratio in the range of $4.81 < \alpha < 7.76$, extended kinks are observed. For $\alpha > 7.76$, the defects are of the odd type [34, 35] and for $\alpha < 4.81$ the crystal exhibits a three-dimensional helix configuration [36]. In the extended defect regime, which is relevant to the current paper, two kinds of defects can be observed. We refer to these defects as horizontal (H) kink and vertical (V) kink. The

two kinks are depicted in Figure 1(c) and (d). The most prominent difference between them is the position of the two inner most ions. In the horizontal case these ions are in the same chain and occupy the same minimum of the Coulomb potential produced by the opposite chain. In the vertical case these ions are in different chains and the ion of the upper chain lies on the potential maximum created by of the lower chain. Another difference is the number of ions in each chain. Ignoring the first 4 ions on the left and right side of a crystal, as they are still close to the linear chain, a crystal with a V kink displays equal ion numbers for both chains. A crystal with an H kink exhibits a two ion difference between the chains. The kink is found in the center of the crystal, due its inhomogeneity [35]. In our experiments, both defects are created in a rf quench and are initially of odd type. They change to the extended type when the rf amplitude is lowered further [35, 37]. The overall probability to create a defect is around 30 %, but only the H defect is used in the experiments, because only this defect shows a soft mode, if it is unperturbed, as we will show in Section 2.4. Therefore, roughly 15 % of all quenches result in a crystal with the necessary extended defect. An experimental image is shown in Figure 1(e). The observed crystal configurations are highly symmetric due to the well controlled environment provided by the ion trap.

2.2. Structural symmetry breaking

For a finite system a symmetry breaking is expected at the Aubry-type transition [12, 13]. In the experiment we observed several fluorescence spots in the symmetry broken regime, as can be seen in Figure 2(a) for $\alpha = 7.21$, where fluorescence spots belonging to the same configuration are indicated by circles. The symmetry breaking is a direct result of the emerging barriers in the Peierls-Nabarro (PN) potential [10] at the critical value of the control parameter, α_c . This potential describes the collective dynamics of a discrete non-linear system. In our case, the PN barrier rises in the center of the crystal, see Figure 2(c). As a result, the extended defect destabilizes and slips into the adjacent minimum of the PN potential, which alters the ion positions and breaks the axial mirror symmetry of the crystal. The finite temperature of the ions results in switching between stable configurations, and hence multiple spots per ion are observed during a finite exposure time of a few tens of ms. The barrier between the minima in the PN potential are on the order of 1 mK to 2 mK, comparable to the temperature of the crystal, which we estimate to be in the low mK regime [37]. We quantify the symmetry breaking by choosing an order parameter Φ , defined as the sum of the relative axial differences between next-neighbor

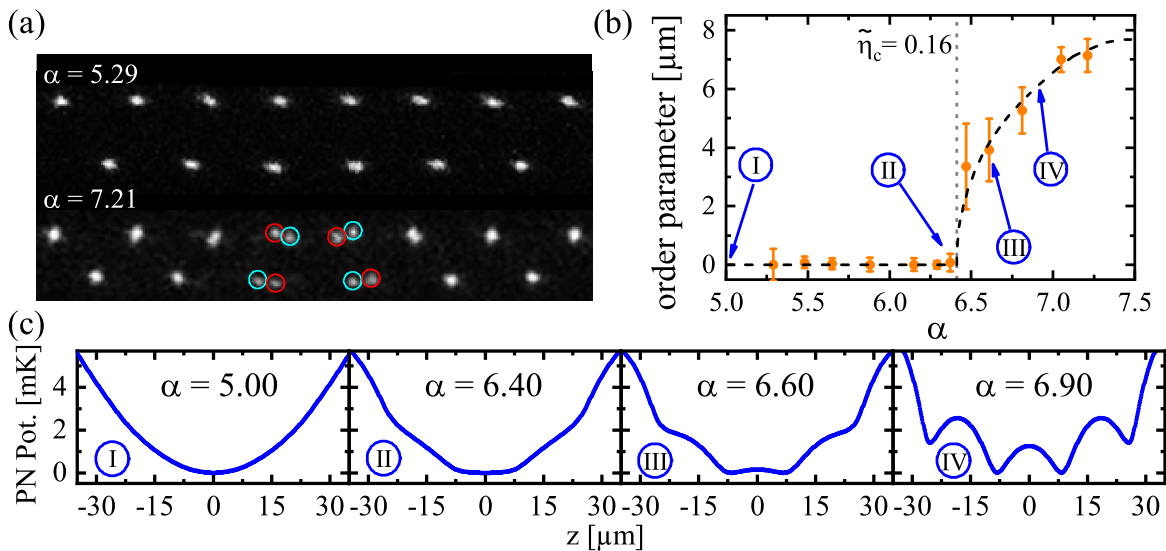


Figure 2. Symmetry breaking at the pinning to sliding transition. (a) Experimentally observed crystal configurations below the Aubry-type transition, at $\alpha = 5.29$, and above, at $\alpha = 7.21$. The images are taken with 700 ms exposure time. The crystal is at a finite temperature in the mK regime, which leads to multiple fluorescence spots above $\alpha_c = 6.41$, as the topological defect moves between the different stable positions. An angle of 40° between the crystals xz plane and the CCD chip, results in apparent smaller radial distances. (b) Absolute order parameter $|\Phi_{\text{red}}|$ against the trapping ratio α . Experimental data (orange circles) and numerically obtained values for $T = 0\text{K}$ (black dashed line) are shown. Experimental data represents a weighted average over 5 to 26 measurements per point, with exception of $\alpha = 7.21$, where only 2 configurations were observed. Error bars are given as one standard deviation weighted by fit errors. The critical point is $\alpha_c \approx 6.41$ (approximate critical corrugation parameter $\tilde{\eta}_c \approx 0.16$). (c) Peierls-Nabarro potential for different trapping ratios α . The increasing PN barriers lead to the symmetry breaking of the system. Barriers for $\alpha > \alpha_c$ are on the order of the temperature in the system, leading to multiple observed ion positions as the defect can move between different minima.

ions from different chains

$$\Phi = \sum_{i \in \text{Chain 1}} \text{sgn}(z_i) \cdot \min_{j \in \text{Chain 2}} |z_i - z_j|, \quad (2)$$

where z_i is the axial coordinate of the i th ion and $z = 0$ is the axis of symmetry for $\alpha < \alpha_c$. Below the transition the order parameter is 0. From numerical simulations, which are described in detail in Section 2.4.2, we extract stable crystal configurations, which yield the order parameter shown in the dashed line of Figure 2(b). The critical point is $\alpha_c \approx 6.41$, at which Φ exhibits a sudden cusp. The corresponding approximate critical corrugation parameter $\tilde{\eta}_c$ is 0.16, which is different from 1, since it is only a rough estimate. Taking fluorescence images of crystals at various ω_x , we extract the ion positions via fitting the fluorescence profile of the individual ions to a Gaussian function. To avoid errors due to optical aberrations far away from the optical axis and to reduce accumulated fitting errors, we do not use the full version of Equation (2). The reduced order parameter $\Phi_{\text{red}} = \Phi_{i=N/2} + \Phi_{i=N/2+1}$ only includes the two central terms, which have the largest contribution to Φ . The value of α_c is not influenced by the choice of Φ . The experimental results are plotted as orange circles in Figure 2(b), and they agree well with the numerical calculations. The error bars are one standard deviation

weighted by the fit errors. Measuring Φ for $\alpha > \alpha_c$ close to the critical point is limited by the resolution of the EMCCD camera, as the fluorescence spots of two configurations need to be at least 2 pixel apart in order to be identified as distinct configurations.

2.3. Derivation of the hull function in a self-organized system

The symmetry breaking in finite systems is also accompanied by the more general breaking of analyticity of the hull functions [12]. In the following paragraphs we will discuss the hull function and its numerical calculation in our model system in more detail.

In the Frenkel-Kontorova model the hull function parameterizes the reachable ground state configurations of an incommensurate system [10, 11]. If the system is below the Aubry or Aubry-type transition, i.e. free sliding, this function is continuous and analytic. Intuitively this means, that during a sliding process of the chain over the potential, all individual particle positions are a realization of a ground state of the system. This changes when the Aubry transition is crossed, and the system start to exhibit stick-slip motion. Certain positions are unstable and not part of the set of ground state solutions, resulting in a discontinuous hull function with broken analyticity [11]. This

property of incommensurate sliding systems exists in both infinite and finite systems, though the two cases are not identical.

In the classical FK model the corrugation potential is not influenced by the particle chain residing above it, which leads to a straightforward representation of the hull function. It is defined as an implicit function $z_j(z_{j,0})$, where z_j is the position of j th ion in the presence of the corrugation potential and $z_{j,0}$ is the position of the j th ion in the absence of the corrugation potential [10]. The particle positions can be calculated with the help of a force F , that pushes the chain along the axial direction. Doing this calculation with and without a corrugation potential yields z_j and $z_{j,0}$, which determine the implicit relation $z_j(z_{j,0})$. Such a procedure is possible, because the corrugation strength U_0 can be set to zero without altering the interaction between chain particles. For a self-organized system, like a two-dimensional ion Coulomb crystal, this approach does not work, because the corrugation potential is part of a back-acting system. Removing it without changing the dynamics of the interaction between particles of the same chain is impossible.

However, in a harmonically trapped system, one can push the complete crystal with a force F , leaving the local ion interactions unchanged, to obtain a relation between the force and the unperturbed coordinates, $z_{j,0}(F)$. Applying an axial shear force ΔF onto the chains, slides the particles over the corrugation potential, leading to perturbed positions $z_j(F)$. The shear force is such that one chain is pushed by $+F/2$, while the other chain is pushed by $-F/2$. Then the relative force between the chains is equal to F , which was used to push the whole crystal. The unperturbed and perturbed coordinates are related via the applied force F , providing a representation of the hull function $z_j(z_{j,0})$. The hull functions for the two ions at the center of the crystal, ion 15 and 16, are shown in Figure 3(c).

In the hull function various gaps open up above the transition due to stick-slip events. These events result from the emergence of the PN barriers above the AT transition, which destabilize crystal configurations, as can be seen in Figure 2(c). The central gap seen in Figure 3(c) for $\alpha > 6.41$ is a direct result of a slip event of the 15th or 16th ion, see Figure 3(a). If the slip event takes place at the position of the defect, the opening in the hull functions is called the primary gap. The non-central gaps in the hull functions of the 15th and 16th ions are either remnants of a slip event of other ions or the defect leaving the crystal. If the defect leaves the crystal, a part of the crystal will reorient itself affecting the positions of the central ions. This is observed, for instance, far below the transition at

$\alpha = 5.65$ and $z_{j,0} \approx 0.15a$, where a is the axial spacing between the 14th and 17th ion, which we consider as a pseudo lattice constant for the crystal center. As the pure zigzag has mostly matched chains, no further information about the AT transition can be gained for bigger forces. Here we note, that, even though the individual ions moved less than a third of a lattice period ($\Delta z < 3 \mu\text{m}$), they have rearranged in a way such, that the defect already left the crystal, which means it moved more than $50 \mu\text{m}$. This illustrates why charge transport is facilitated by topological defects [38].

For $\alpha = 6.38$, still below α_c , more than one gap can be seen in the hull function. One in each function is due to the defect leaving the crystal. The others are secondary gaps due to stick-slip events, even though the system is globally in the sliding regime. The stick-slip events occur, because of the inhomogeneity of a harmonically trapped crystal, which reduces the charge density towards the edge of the crystal, as illustrated in Figure 3(b). This increases the corrugation depth between the ion chains, as the axial distance between ions grows, while the radial distance between the chains decreases. Therefore, the critical point is locally already crossed, if the local ordering is disturbed by a topological defect. The slip events from these ions are seen by the central ions 15 and 16, which gain gaps in their hull functions as a result. In a crystal with equidistant ions, the secondary gaps will only exist above α_c , as only this regime stick-slip motion is present.

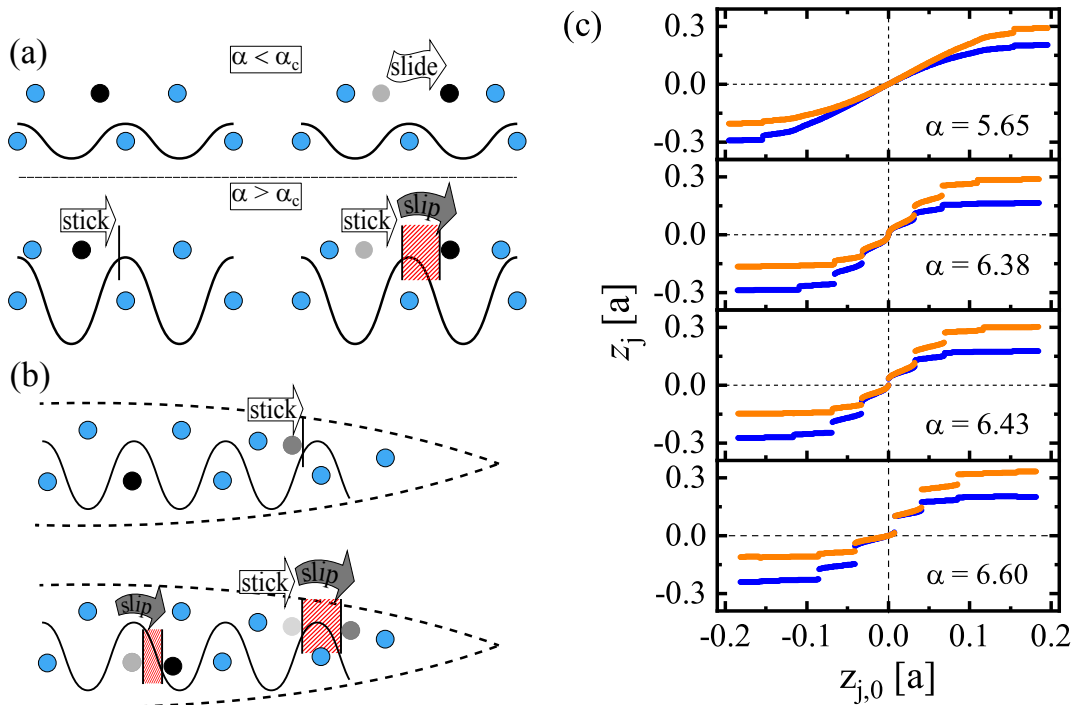


Figure 3. Hull function of an inhomogeneous crystal. (a) Schematic explanation of a primary gap in the hull function. For $\alpha < \alpha_c$ a particle (black circle) can assume all positions, when being pushed. In the hull function no gap is observed. For $\alpha > \alpha_c$ the corrugation is stronger, and several positions are unstable. A slip occurs and a gap appears in the hull function. (b) Secondary gap in the hull function. Due to the Coulomb interaction, a slip of an outer ion (dark gray circle) changes the observed inner ion (black) position suddenly and a gap in the hull function appears. In an inhomogeneous system this can also happen, if $\alpha < \alpha_c$, because the chains are closer together near the crystal edge. (c) Numerically calculated hull functions. The functions are shown for the 15th (orange) and 16th (blue) ion for different values of the control parameter α . The gaps for $\alpha = 5.65$ are due to the topological defect leaving the crystal. The inner gaps for $\alpha = 6.38$ are due to stick-slip events away from the center. The primary gap opens up in the center of the hull functions for $\alpha > \alpha_c = 6.41$. All positions are in units of the pseudo lattice constant a , the distance between the 14th and 17th ion.

2.4. Motional mode frequency of the topological defect

The localized vibrational mode of the topological defect drives the AT transition [19]. The lower its frequency, the lower the energy required, to move the chains against each other. This defect mode is one of the gapped modes, previously considered for quantum information [29]. Excitation of the high energy gapped was shown in [31]. Here we are interested in the low energy gapped mode and how the mode frequency depends on the corrugation strength of the sliding system.

2.4.1. Spectroscopy Experimentally we measure the vibrational mode frequency via amplitude modulation of a laser addressing the $^2S_{1/2} \rightarrow ^2P_{1/2}$ transition. This exerts a periodic force

$$F_p = \frac{F_0}{2} [\cos(2\pi \cdot \nu t) + 1] \quad (3)$$

on the crystal, where $F_0/2$ is the amplitude of the modulation, which depends on the power of the laser and the detuning from the atomic resonance, and ν is the modulation frequency. F_p can excite a motional

mode k , if ν is close to a mode frequency $\nu_k = \omega_k / (2\pi)$. Additionally, the intensity distribution of the laser \mathbf{A} must overlap with the mode vector $\boldsymbol{\mu}_k$. This means, that the scalar product $\boldsymbol{\mu}_k \cdot \mathbf{A}$ has to be non-zero. The laser used in our experiments has an angle of 25° to the crystal axis and an approximate angle of 50° to the xz plane of the crystal. The beam has a Gaussian beam profile with waist of roughly $80 \mu\text{m}$ in both directions. If the beam is centered on the crystal, the intensity distribution will be identical for both chains. This would result in a zero overlap with the localized defect mode of the crystal, as both chains are excited with the same force and in the same direction. If the intensity maximum is focused radially on one of the chains, see Figure 4(a), then an intensity difference between the chains exist, which results in a non-zero scalar product, $\boldsymbol{\mu}_k \cdot \mathbf{A}$, enabling the excitation of this mode. To determine the resonance, ν is scanned at a rate of 1 kHz s^{-1} to 2 kHz s^{-1} and the spread of the fluorescence of the central ions is recorded with the EMCCD camera. An example image of the excited defect mode is shown in Figure 4(b). Only the central ions move with a significant amplitude, illustrating

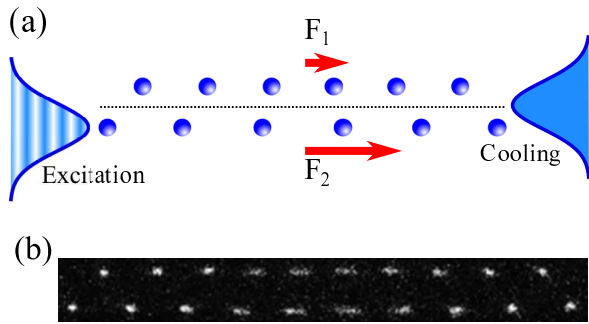


Figure 4. Vibrational mode spectroscopy. (a) Excitation method. The ion crystal is illuminated by a centered laser beam, which continuously cools the ions. A second, axially focused laser beam is centered on one chain, in order to realize a difference in the light forces acting on the chains. The laser is amplitude modulated. (b) Excited shear mode. CCD image with an excited localized defect mode at $\alpha = 5.77$. Exposure time is 100 ms and cooling laser power of 300 μW . The power of the focused laser was modulated with a frequency of (12.1 ± 0.3) kHz between 0 μW and 35 μW .

that the excitation is localized on the defect. The resonance is measured with an uncertainty of 300 Hz to 400 Hz, which can be improved by a slower frequency scan rate and recording more images per scan. The applied amplitude $F_0/2$ on the crystal needs to be big enough to actually excite observable motion but also has to be small enough, to limit non-linear excitations. In our experiment we found that an amplitude $F_0/2$ corresponding to a maximum beam power of $P_0 = 20 \mu\text{W}$ is enough to excite motion near the phase transition. While exciting the motion with the focused laser beam, the ions were still illuminated with a spatially extended cooling beam. This beam damps the dynamics introduced via the amplitude modulation. Typical powers of the cooling beam while conducting spectroscopy are 200 μW to 300 μW .

2.4.2. Numerical calculations Firstly, we look at the expected mode frequency in dependence on the control parameter α . For this, we analyze the total potential energy of N harmonically trapped ions in two dimensions:

$$V = \sum_{i=1}^N \frac{m}{2} (\omega_x^2 x_i^2 + \omega_z^2 z_i^2) + \frac{e^2}{4\pi\epsilon_0} \sum_{i=1}^N \sum_{j<i} |\mathbf{r}_i - \mathbf{r}_j|^{-1}, \quad (4)$$

where x_i and z_i are the coordinates of i th ion in the coordinate systems defined in Figure 1(a); ω_x and ω_z are the harmonic trapping frequencies; and $\mathbf{r}_i \equiv \{x_i, z_i\}$. The third dimension is neglected, due to the anisotropy of the radial secular frequencies. We obtain the frequency of the topological defect mode (and any

other mode) by numerically diagonalizing the Hessian matrix

$$H_{i,j} = \left. \frac{\partial^2 V}{\partial q_i \partial q_j} \right|_{\mathbf{q}(0)}, \quad (5)$$

where V is the total potential energy given by Equation (4), q_i are the degrees of freedom and $\mathbf{q}(0)$ is a given equilibrium configuration. The stable equilibrium configuration, $\mathbf{q}(0)$, is obtained by numerically solving the equations of motions under high damping. There are $2N$ vibrational normal modes in a two-dimensional ion crystal with N ions. The k th eigenvector of H_{ij} is the k th normal mode of the crystal $\boldsymbol{\mu}_k$, and the corresponding eigenvalue λ_k determines the mode frequency via the relation $\omega_k = \sqrt{\lambda_k/m}$. The localized defect mode has the lowest frequency for $\alpha < 7$, and it drives the symmetry breaking transition. Figure 5(b) shows the shear mode frequency as a function of α for different numbers of ions N . The frequency tends to zero near the critical point $\alpha_c \approx 6.41$ (6.08, 6.74) for $N = 30$ (28, 32), while increasing both above and below α_c , because of the finite size of the system. The critical point α_c depends on the ion number N . The more ions are present, the stronger is the repulsive Coulomb force, and therefore the more radial confinement, and subsequently higher α , is necessary to bring the chains close enough together to observe the AT transition. In a previously installed prototype trap [39], we observed the dependence of the defect mode frequency on N , but with consistently lower frequencies, than the calculations predict. Near the AT transition we observe a difference between the measured and calculated frequencies in both the high-precision and the prototype trap. This discrepancy stems mainly from the missing temperature effects in the numerical calculations.

In order to investigate the effect of a finite crystal temperature, we conduct three-dimensional molecular dynamics simulations of an unperturbed crystal (i.e. without laser excitation, but with cooling). These simulations solve the Langevin equations, utilizing an impulse integrator algorithm [40]. The total potential energy of a three-dimensional N ion system is

$$V = \sum_{i=1}^N \frac{m}{2} (\omega_x^2 x_i^2 + \omega_y^2 y_i^2 + \omega_z^2 z_i^2) + \frac{e^2}{4\pi\epsilon_0} \sum_{i=1}^N \sum_{j<i} |\mathbf{r}_i - \mathbf{r}_j|^{-1}, \quad (6)$$

where x_i , y_i and z_i are the coordinates of i th ion ω_x , ω_y , ω_z are the harmonic trapping frequencies; and $\mathbf{r}_i \equiv \{x_i, y_i, z_i\}$. The equation of motion for the j th ion in one dimension is

$$m\ddot{\chi}_j + \nabla_{\chi} V + \eta\dot{\chi}_j = \xi_{\chi j}(t), \quad (7)$$

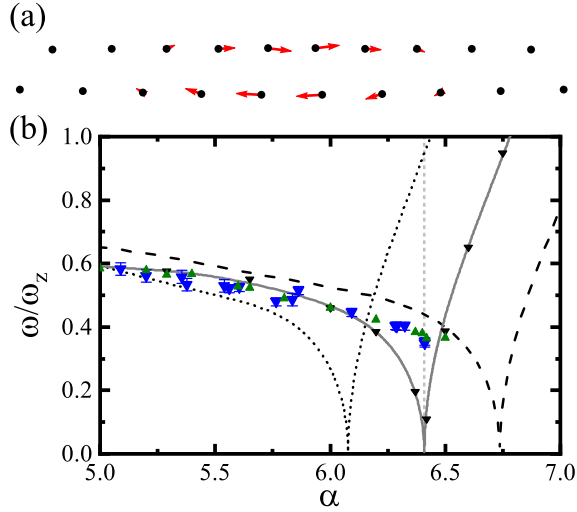


Figure 5. (a) Numerically obtained mode vector. Amplitudes are in arbitrary units and values smaller than 10% of the maximum amplitude are not shown. (b) Mode frequency against the control parameter α . Experimental data taken in the high-precision trap for a 30 ion crystal is plotted as blue triangles. Error bars are given by the uncertainties of the measured common mode and defect mode frequency. Numerical calculations at $T = 0\text{K}$ are shown for $N = 28$ (black dotted line), $N = 30$ (gray solid line) and $N = 32$ (black dashed line). Frequencies obtained via the Fourier transformation of molecular dynamics simulation are shown for $T = 5\mu\text{K}$ (black triangles) and $T = 1\text{mK}$ (green triangles). All angular frequencies are plotted in units of the axial common mode angular frequency $\omega_z = 2\pi \times (25.6 \pm 0.2)\text{kHz}$.

where $\xi_{\chi j}(t)$ is a stochastic force, χ is x , y or z , η is a damping term from laser cooling and V is the total potential energy from Equation (6). The stochastic force fulfills the following two conditions:

$$\langle \xi_{\chi j}(t) \rangle = 0 \quad (8)$$

$$\langle \xi_{\chi j}(t) \xi_{\gamma k}(t') \rangle = 2\eta k_B T \delta_{\chi\gamma} \delta(t-t'), \quad (9)$$

where γ is x , y or z , j and k are ion indices and $\langle \dots \rangle$ indicates time averaging. Equation (9) is the fluctuation-dissipation relation that ensures that the system undergoing the stochastic dynamics equilibrates at temperature T [21]. In these simulations we look at crystals with topological defects for different temperatures T , each time letting the system evolve freely for 10ms. We then analyze the resulting axial trajectory of the 15th ion, $z_{15}(t)$, because this ion has one of the highest mode amplitudes for the localized defect mode in axial direction. Taking the Fourier transform of this trajectory

$$\hat{z}_{15}(\nu) = \mathcal{F}(z_{15}(t)) \quad (10)$$

yields the spectrum of the harmonic motions excited in the crystal dynamics. Figure 6(a) shows the spectrum for a crystal at $T = 5\mu\text{K}$ for different trapping ratios α . The amplitude peak at a frequency of 24.6kHz is due to the excitation of the axial common mode,

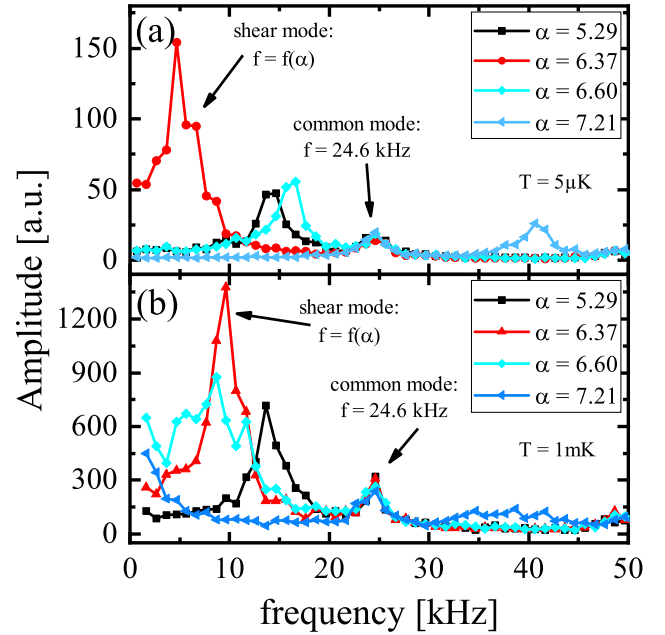


Figure 6. Spectra obtained via Fourier transformation of MD simulations. (a) Spectrum for $T = 5\mu\text{K}$ for different α . Common mode, independent of α , visible at 24.6kHz. The frequency of the defect mode depends on α . (b) Spectrum for $T = 1\text{mK}$. The frequency spread of the defect mode becomes broader the closer the system is to α_c . Above the transition ($\alpha = 6.6$ and $\alpha = 7.21$) a range of several kHz with comparable amplitude is observed. Therefore, no single harmonic oscillation has an observable amplitude.

for which all ions oscillate in phase, and the other amplitude peaks are due to excitation of the topological defect mode at different corrugations. The dependence of the mode frequency on α at $5\mu\text{K}$ is shown with black triangles in Figure 5(b). These results agree with the frequencies obtained from the diagonalization of the Hessian matrix. The observed Fourier spectrum changes, when T is increased. At experimentally realistic temperatures of 1 mK the Fourier spectrum close to, and above, the transition changes, as can be seen in Figure 6(b). The common mode can still be resolved independently of the trapping ratio, but only below α_c we observe distinct peaks for the defect mode in the spectrum. Additionally, these peaks are visible at different frequencies in comparison to the results for $T = 5\mu\text{K}$. For $\alpha > \alpha_c$ a broad range of frequencies with nearly identical amplitudes is seen (for $\alpha = 6.6$ near 10kHz and for $\alpha = 7.21$ near 40kHz), indicating that no single harmonic oscillation is present. This can be explained by the PN potential barriers, which are in the mK range, see Figure 2(c), and small enough for the defect to overcome. During the movement between the minima, the non-linear parts of the PN potential are sampled and many frequency components are part of the dynamics, explaining why the mode of the defect could not be excited with an observable amplitude in

the experiment for $\alpha > \alpha_c$. Furthermore, we find that the frequencies extracted from the Fourier analysis for $T = 1$ mK agree with the experimentally observed frequencies, see Figure 5(b). This indicates that the frequency measurements were limited by the finite Doppler cooling temperature of the ${}^2\text{S}_{1/2} \rightarrow {}^2\text{P}_{1/2}$ transition.

3. Symmetry breaking by external forces

In this section we investigate several external forces on ion Coulomb crystals and how they change the crystal structure and subsequently the mode frequencies. This is of interest for directed transport of kink solitons [31] and the frictional properties, as a change in the soliton mode frequency implies different interaction energies between the chains. In a previously used prototype trap [39], we observed asymmetric crystal configurations and measured lower frequencies of the localized defect mode, than the calculations predict. Therefore, we investigate here trap related forces, such as those stemming from higher order terms in the axial trapping potential and axial micromotion, as well as forces due to laser illumination of the ions. While all effects change the crystal and hence the position of the topological defect, the latter effect offers the possibility to move the defect at will through the crystal.

3.1. Anharmonicities of the trapping potential

As the manufacturing process of an ion trap is limited by its tolerances, the trap potential will contain non-quadratic contributions [41].

Here, we investigate the influence of a third order term in the axial trapping potential on the crystal structure and the frequency dependence on the corrugation. This is done numerically by changing the potential term for the z direction:

$$m\omega_z^2 z^2 \rightarrow m\omega_z^2 (z^2 + C \cdot z^3),$$

where C determines the relative strength of the third order term. The addition of the anharmonic term to the potential perturbs the equilibrium positions of the ions. We define the difference of the axial positions of a modified crystal $z_{j,\text{mod}}$ and the axial positions of an unperturbed crystal $z_{j,\text{pond}}$ as $\Delta z_j = z_{j,\text{anharmonic}} - z_{j,\text{pond}}$, where j is the ion index. We plot the difference in Figure 7. C was chosen such that the resulting equilibrium positions fit best to the positions observed in the prototype trap. The modified confining potential has a higher curvature on one side of the crystal, while the other side has a lower curvature in comparison to the ideal case. One side of the crystal is therefore pushed closer to the center, while the other side is shifted away from it. This change in the axial positions influences the interaction between the ions and thus

modifies the dependence of the localized defect mode frequency on α , see Figure 7(b). In particular, in the presence of the third order term in the axial potential, the mode softening is less pronounced or not present at all, depending on the strength of C .

Up to now we have assumed, that the minimum of the second order term and the saddle point of the third order term are at the same axial position. As far as we know, there is no reason that this is necessary. To match the experimental crystal configuration to the simulation, we include a differential shift z_0 in the position of z^2 and z^3 terms in regard to the crystal structure and the mode frequency, with results shown in Figure 7(c,d). The values of z_0 and C are fitted to the observed crystal configurations, which we also plot in Figure 7(c). Shifting the z^3 term by only $30\ \mu\text{m}$ relative to the z^2 term yields a significantly distorted crystal configuration, in which the left side is pushed towards the center by a few μm , while the right side is only slightly perturbed. In the frequency dependence we observe not only a less pronounced soft mode, but also a shift of the minimum of the localized mode frequency towards higher values of the control parameter α . As it is possible to fit the simulations with anharmonic terms closely to observed crystals in the prototype trap, it is plausible, that the potential of the prototype trap included significant higher order terms. This is most likely due to the manufacturing process, as the prototype trap was milled, resulting in slightly asymmetric trap segments.

Both the anharmonic potential itself and the shift from the harmonic part lead to an intrinsic symmetry breaking and a change of the defect mode frequency near the transition. It is therefore necessary to suppress anharmonic potential terms in an ion trap, for experiments, that require high symmetry of the crystal. The higher order terms can be minimized by the design and careful construction of the trap.

3.2. Micromotion

As all investigations take place in a 2D crystal, where most ions are situated in a non-zero rf field, the micromotion induced by the oscillating trapping field changes the structure and the dynamics of the ion crystal in comparison with the ponderomotive approximation [42]. Furthermore, due to the finite size of the segmented linear Paul trap there are electric field gradients from the rf fields along the axial direction. This additional gradient induces axial micromotion, which might also influence the crystal.

The dynamics of ions trapped in a rf field are described by the Mathieu equations [43]. Solving these equations for a 30 ion crystal containing a defect at a radial trapping frequency $\omega_x = 132$ kHz and comparing it to the ponderomotive approximation, reveals differ-

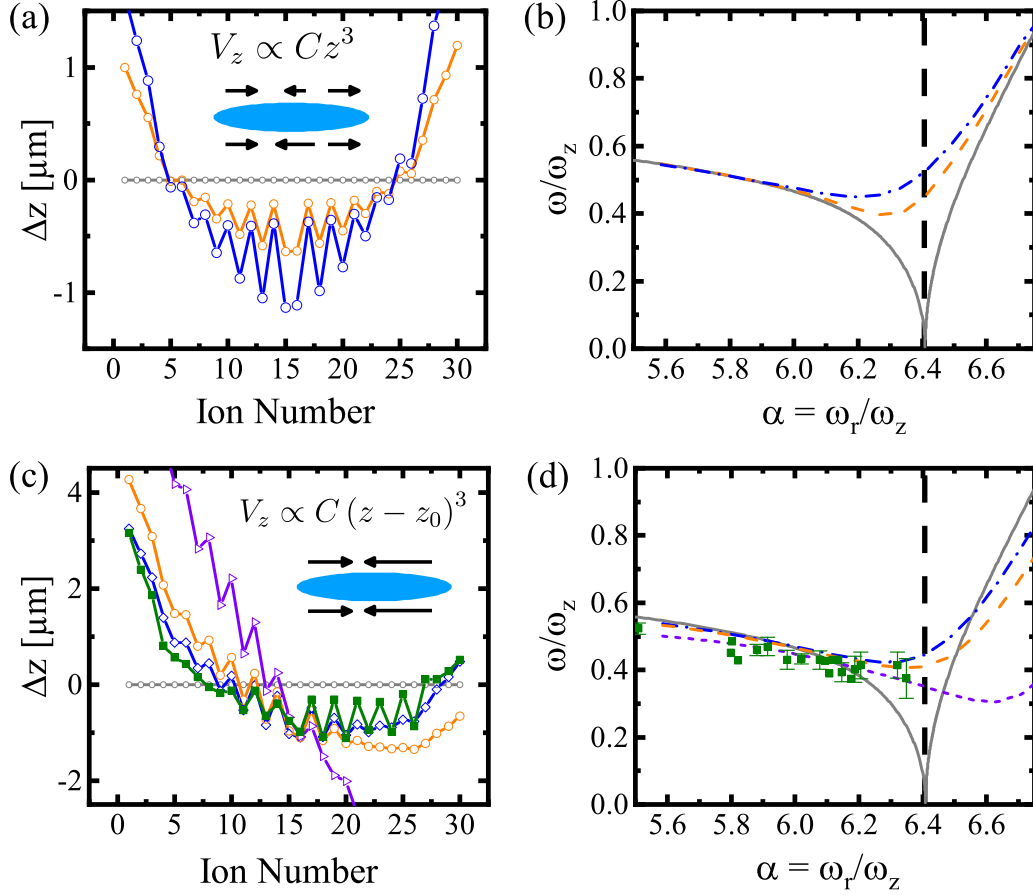


Figure 7. Influence of anharmonic potentials on the crystal symmetry and frequency dependence of the defect mode in comparison to experimentally observed crystal configurations and frequencies (green filled squares). The blue ellipsoids sketch the deformation of the axial ion positions over a crystal. (a) Difference in axial position Δz between the modified equations with a third order term in the axial trapping potential and the unperturbed ponderomotive solution. Shown are numerical simulations for $C = 0$ (i.e. no perturbation, gray empty dots) $C = -170 \text{ m}^{-1}$ (orange empty dots) and $C = -300 \text{ m}^{-1}$ (blue empty dots). $\alpha = 5.51$. The ions on the left side are closer to the center, while the ions on right side are moved away by this perturbation. (b) Defect mode frequencies against control parameter for an anharmonic axial potential. Color scheme identical to (a). The modified crystal leads to a non vanishing of the mode frequency at α_c . (c) Change in the axial coordinate for a spatial shift of the anharmonic potential with respect to the harmonic potential. Numerical simulations for z_0 of 0 (i.e. no perturbation, gray empty dots), 30 μm (blue empty diamonds), 50 μm (orange empty circles) and 150 μm (violet empty triangles), as well as experimental data (green squares) taken in the prototype trap. $\alpha = 5.51$. All calculations have been carried out with $C = -300 \text{ m}^{-1}$, expect for $z_0 = 0$, where C was also 0. (d) Defect mode frequencies against control parameter for a spatial shift between harmonic and anharmonic part of the axial potential. Color scheme identical to (c). No vanishing of the mode frequency is observed and the position of the minimal frequency is shifted.

ences $\Delta z_j = z_{j,\text{Mathieu}} - z_{j,\text{pond}}$ of less than 200 nm in the z coordinates of the ions. If axial micromotion with an electric field gradient $|\nabla E_{\text{rf},z}|$ of 2% of the radial electric field gradient $|\nabla E_{\text{rf},r}| = 3.2 \times 10^8 \text{ Vm}^{-2}$ is also present, then the crystal is axially compressed, see Figure 8(a). The further away an ion is from the center of the trap, the further its position is changed by the micromotion. Because the rf gradient changes sign in the center of the trapping region it acts like an additional axial potential, as long as the crystal is in the center of the trapping region. In the prototype trap the axial micromotion has an electric field gradient of $|\nabla E_{\text{rf},z}| = 1.9 \times 10^6 \text{ Vm}^{-2}$, which is roughly 0.6% of the radial electric field gradient $|\nabla E_{\text{rf},r}|$ [39] and in

the precision trap we observe only an electric field gradient of $|\nabla E_{\text{rf},z}| \approx 6.4 \times 10^4 \text{ Vm}^{-2} \approx 2 \cdot 10^{-4} \cdot |\nabla E_{\text{rf},r}|$ along the axial direction [44]. For both traps, the calculated differences Δz_j are nearly identical to the simulations without any axial micromotion, making the effect negligible. In the radial direction the effect of axial micromotion is small in comparison. In Figure 8(b) we plot the difference in the x coordinate. For a high axial micromotion of $2\% \cdot |\nabla E_{\text{rf},r}|$ the difference in radial coordinates Δx_j due to the axial micromotion are less than 100 nm. Using the axial electric field gradients from both traps, we again do not observe a difference to the simulations without any axial micromotion.

The mode frequencies were not calculated for

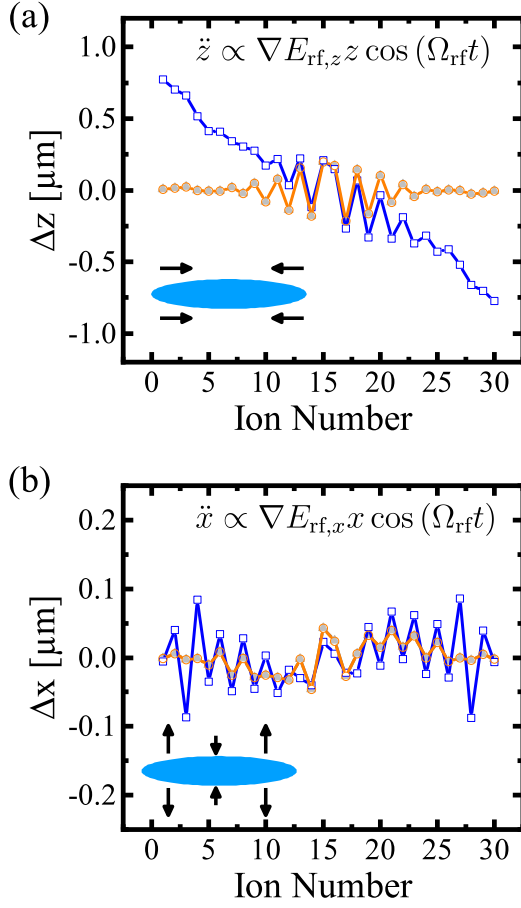


Figure 8. Influence of micromotion with and without axial rf gradients. (a) Axial difference of ion positions for crystals calculated from the Mathieu equations and the ponderomotive approximation. The numerical calculations for an axial rf field gradient $\nabla E_{\text{rf},z}$ of $6.4 \times 10^6 \text{ Vm}^{-2}$ (blue empty squares), $6.4 \times 10^4 \text{ Vm}^{-2}$ (orange empty circles, high precision trap) and for no axial micromotion (gray triangles) are shown. The result for the high-precision trap is identical to the result for no axial micromotion. (b) Radial difference between the ion positions. Color code identical to (a). The blue ellipsoids sketch the deformations of the axial and radial ion positions over a crystal for $\nabla E_{\text{rf},z} = 6.4 \times 10^6 \text{ Vm}^{-2}$. For both graphs: $\alpha = 5.51$.

this effect, as the simulation using the full Mathieu equations does not yield a static solution needed for the Hessian matrix approach. It is possible to calculate the normal mode spectrum using the Floquet-Lyapunov approach [42, 45], but this is outside of the scope of this paper. The influence of micromotion is only relevant for traps with an axial rf field gradient higher than 0.6% of the radial rf field gradient. This gradient can only be suppressed by the design and careful manufacturing of the trap [33].

3.3. Differential light forces

Illuminating ions with near resonant light will lead to an average force acting on them. These light forces will

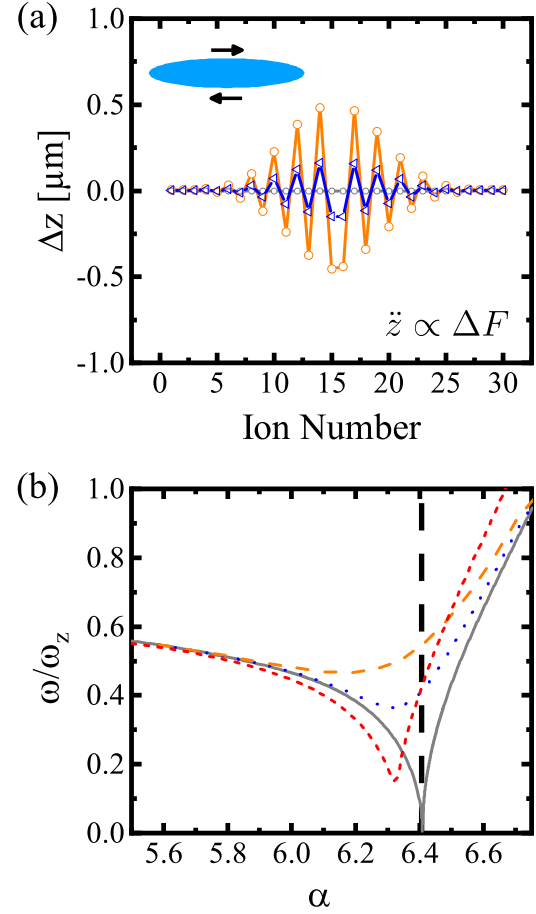


Figure 9. Influence of light forces. (a) Difference in axial position from the ideal crystal Δz for differential light forces ΔF of $0.9 \times 10^{-21} \text{ N}$ (blue diamonds) and $2.7 \times 10^{-21} \text{ N}$ (orange circles) from numerical simulations. For comparison an ideal crystal is shown as gray circles. $\alpha = 5.51$. The blue ellipsoid sketches the deformation of the axial ion positions over a crystal. (b) Frequency dependence on the interaction strength for applied differential forces. Shown are results for $\Delta F = 0.9 \times 10^{-21} \text{ N}$ (dotted blue line), $2.7 \times 10^{-21} \text{ N}$ (orange dashed line) and $9.8 \times 10^{-21} \text{ N}$ (red short-dash line).

in general modify the crystal structure, but as long as the illumination is uniform on the crystal, they will only shift the center of mass. An illumination that leads to an axial differential force between the two ion chains will move the topological. The position of the topological defect is sensitive to forces in the 10^{-21} N level.

In the experiments we use two focused cooling laser beams, one for cooling and detection and another for vibrational mode excitation, see Section 2.1 and Section 2.4. A typical zigzag configuration in our setup has a radial separation of the ion chains of approximately $15 \mu\text{m}$ and has a 45° angle to the beam wavefront, leading to an apparent separation of $10.6 \mu\text{m}$, which is not much smaller than the radial beam waist of approximately $80 \mu\text{m}$. Any

alignment of the radial beam, that results in non-uniform illumination between the ion chains, will lead to a differential force $\Delta F = F_1 - F_2 \neq 0$ along the axial direction, where $F_{1,2}$ is the force along z acting on chain 1 and chain 2, respectively. From numerical simulations we find, that such a differential force will move the topological defect inside the crystal. This can be actively used, to investigate charge or information transport in ion Coulomb crystals [29], as well as further investigations into nanofriction of two sliding chains. In Section 4 we investigate in detail, what such a movement entails.

When applying differential forces to the crystal, the localized kink mode frequency near the phase transition will change. For different ΔF we plot the change in the axial crystal structure in Figure 9(a) and the expected frequency dependence on α in (b). This can be understood by examining the Peierls-Nabarro potential, shown in Figure 2(c). The potential is overall confining due to the inhomogeneity of the crystal, and it contains PN barriers above the AT transition. The overall positive curvature of the PN potential explains why a finite frequency below the AT transition exists. This positive curvature is balanced by the negative curvature of the emerging PN barrier at $z = 0$ when the system is near the phase transition, resulting in near zero frequency of the localized mode. However, when differential forces are applied, the kink soliton is shifted away from the point, where a PN barrier is formed. This leads to the observed non-zero harmonic frequency. Increasing ΔF further, results again in a soft mode behavior of the defect frequency, see Figure 9(b) for $\Delta F = 9.8 \times 10^{-21}$ N.

In our setup, working with a waist of $80 \mu\text{m}$, the maximum differential light force due to a laser beam on a zigzag crystal is achieved, if the radial crystal center is situated near the maximum slope, i.e. at $z \approx \pm w/2$, of the Gaussian intensity distribution $I(z) = I_0 \exp(-2z^2/w_0^2)$. As an example, if a crystal is placed on the slope, ΔF around 2.1×10^{-21} N can be reached with an effective power $P_e = P_0/2$ of $10 \mu\text{W}$. From the numerical simulations we gather, that such forces result in a finite minimum of the mode frequency. For the frequency measurement we needed to have a slight differential light force in the laser beam, so that it can excite the axial shear mode. For this we adjusted the intensity maximum of the laser beam to one of the chains, resulting in roughly 6% intensity difference between the rows. We expect the resulting differential force to increase the minimal frequency to $0.32\omega_z$. This is currently below the measured frequency and is not yet limiting the experiments. Since a lower mode frequency needs smaller ΔF to excite the motion, this future limitation can be prevented by reducing laser power or reducing the intensity difference between

the chains.

To avoid distortion of the crystal structure it is therefore necessary to symmetrically center the laser beam onto the ions, minimizing differential light forces.

4. Motion of the topological defect

In this section we discuss the motion of the topological defect, when the chains are pushed by differential forces introduced in the previous section. We will look at the motion for both the horizontal and vertical kink, and compare their behavior.

Starting with the frequency of the vibrational defect mode for the vertical kink we find, that in contrast to the horizontal topological defect, it does not exhibit a soft mode tending to zero, see Figure 10, or a symmetry breaking at the critical point. This can be explained by examining the PN potentials shown in Figure 11. For $\alpha > \alpha_c$ the PN potential of the vertical kink has a minimum in the center of the trap, whereas the horizontal kink has a maximum. When the transition is crossed, the vertical kink does not move spontaneously, because the global minimum before the transition is still the global minimum after the transition.

By varying the force difference ΔF we push the kink through the crystal; the higher the $|\Delta F|$ the larger is the displacement of the kink from the center. We find that the local structure of a stable kink configuration changes periodically as a function of ΔF , as is shown in Figure 12(a) and (b). If ΔF is around 5×10^{-21} N, the local structure of a vertical defect looks like a horizontal defect. If the force is increased further to roughly 10×10^{-21} N, the initial local structure is reproduced, but one lattice period away from the initial position. Shown in Figure 12(c) is the soft mode frequency, i.e. the lowest frequency of the localized defect mode, against an applied ΔF . In this relation a similar periodic behavior is observed.

We find, that the minimum mode frequency is low (tending towards zero), whenever the local structure looks like a H defect. The minimum is high (around $0.5\omega_z$), when the defect is locally similar to the V defect. By starting with an H defect we observe the opposite behavior. This explains, why a differential force ΔF 'destroys' the soft mode. The local structure changes from an H defect to a V defect, which does not exhibit a soft mode.

Even though these calculations are done for static configurations, in a dynamic process, the ions will move along the same trajectory. Therefore, we conclude, that the motion of the extended kink in an ion Coulomb crystal is accompanied by a change in the nature of the defect, which can be seen both in its local structure and in the frequency of the vibrational defect mode.

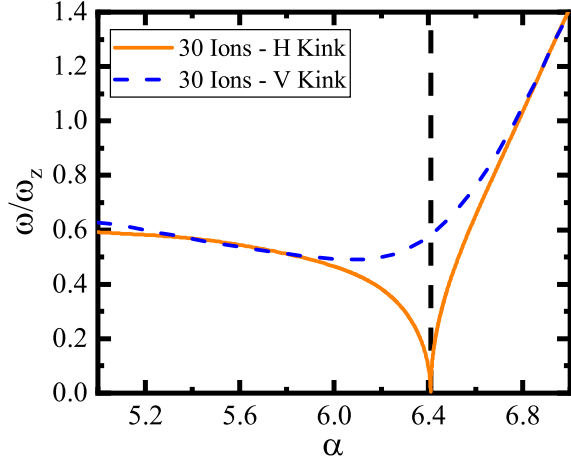


Figure 10. Defect mode frequency for different defect types. Plotted are the relation between mode frequency and control parameter α for the horizontal (orange solid line) and the vertical (blue dashed line) defect.

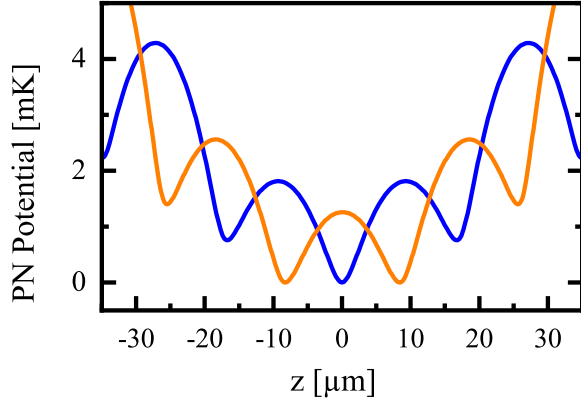


Figure 11. Peierls-Nabarro potential for both extended defects above α_c . The PN potential for the horizontal defect (orange line), shows a PN barrier, at the center of the crystal. The PN potential for the vertical defect (blue line) shows no PN barrier at the center part of the crystal.

Note that the vertical and horizontal defect are still distinguishable by their number of ions per chain. Only locally they shift into each other.

5. Discussion and Conclusion

In this work, we investigated atomic friction in self-organized ion Coulomb crystals with topological defects. We observed the Aubry-type transition from the sliding to the pinning regime and demonstrated experimentally and numerically the two main features of this transition, namely the symmetry breaking and the existence of a soft mode. The excitation of the low energy gapped mode of the topological kink soliton was experimentally demonstrated and its frequency was measured as a function of the distance between the

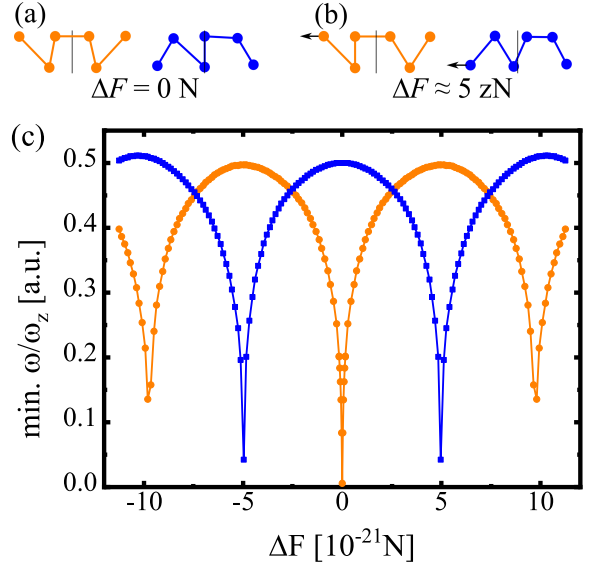


Figure 12. Shear forces move and change topological defects. (a) Local topological defect structure for a horizontal (left, orange) and a vertical defect (right, blue) for $\Delta F = 0$. (b) Local defect structure for a horizontal and a vertical kink for $\Delta F \approx 5 \times 10^{-21}$ N. (c) Numerically obtained minimum of the soliton mode frequency in dependence of an applied force difference ΔF for the horizontal (orange circles) and vertical (blue squares) defect. For increasing ΔF the mode frequency of the horizontal defect becomes finite. A further increase leads to a reduction of the soft mode frequency again. The original crystal structure is reproduced at the next lattice site. This behavior repeats for each lattice site. The vertical kink shows the opposite behavior.

two chains, which directly relates to the interaction energy between them. These findings are of direct relevance to research that aims to exploit topological defects for quantum information processing [29]. The experimental observation of the mode softening at the Aubry-type transitions was limited by the finite temperature of the crystal, which leads to shifts of the mode frequencies. Molecular dynamics simulations demonstrate that lower temperatures, of the order of μK , are necessary to observe a strong softening of the defect mode. The spectroscopic method, introduced in this work, for probing the vibrational mode of the topological defect with the help of amplitude modulated laser light is an alternative to typical excitation methods, such as parametric excitation via rf modulation [31, 46]. It offers the advantage of being mode sensitive as the laser intensity distribution can be matched to fit a specific motional mode vector, providing a tool for investigating mode mixing in ion Coulomb crystals.

We also numerically investigated the influence of external forces, present in ion trapping experiments, on the crystal structure and the kink soliton frequency. The sensitivity of the kink to these effects, can be used to characterize even small disturbances in ion

trap experiments. We were able to fit the experimental results, obtained in a previously used milled prototype trap [39], closely to simulations which include an additional third order term in the axial potential. The additional non-linear term is most likely due to the fabrication method. In the new high-precision, laser-cut ion trap [44], an influence of higher order terms was not observed. We also investigated the influence of axial micromotion on the crystal configuration and found that, for experimentally observed values of micromotion, the ion positions are not changed in comparison to simulations using no axial micromotion. It is known that mode frequencies obtained from the ponderomotive approximation deviate by a few percent to frequencies obtained from the full dynamics [45]. However, as the relative experimental resolution of our method is currently around 4%, it is unlikely that we could resolve this frequency difference. In future experiments, the resolution can be improved, in which case using the Floquet-Lyapunov approach to calculate the mode frequencies might be necessary.

With the help of differential light forces, of only a few 10^{-21} N, the topological defect can be moved through the crystal. This effect is similar to force gradients due to anharmonic potentials, when directed transport was observed [31]. We observed a periodic change in the local structure of the kink as a function of the applied external force, demonstrating that as the kink moves through the chain it alternates between two types of stable kinks, one with a gapped vibrational mode (vertical kink) and the other with a soft vibrational mode (horizontal kink).

In future experiments, the crystal temperature can be lowered to the μ K regime, using dark resonances [47–49], Sisyphus cooling [50] via polarization gradients or narrow transitions [39,44] in other ion species implanted into the crystal. Lower temperatures might enable friction experiments in the quantum regime [51]. Furthermore, investigations of crystals of higher dimensions or homogeneously spaced crystals can help in translating the results from our model system to solid state sliding systems. Here the versatility of ion traps can help, as either designed anharmonic potentials or ring traps [52] could be used to create such scenarios.

Acknowledgments

We thank Jonas Keller for many useful discussions and valuable help with the experiment control. We thank Lars Timm for carrying out numerical calculations and for comments on the manuscript. This work was supported by the DFG through grant ME 3648/1-1.

References

- [1] Vanossi A, Manini N, Urbakh M, Zapperi S and Tosatti E 2013 *Rev. Mod. Phys.* **85** 529
- [2] Kudernac T, Ruangsupapichat N, Parschau M, Maciá B, Katsonis N, Harutyunyan S R, Ernst K H and Feringa B L 2011 *Nature* **479** 208
- [3] Kühner F, Morfill J, Neher R A, Blank K and Gaub H E 2007 *Biophysical Journal* **92** 2491–2497
- [4] Ward A, Hilitki F, Schwenger W, Welch D, Lau A, Vitelli V, Mahadevan L and Dogic Z 2015 *Nat. Mater.* **14** 583–588
- [5] García-Mata I, Zhurov O and Shepelyansky D 2007 *Eur. Phys. J. D* **41** 325–330
- [6] Benassi A, Vanossi A and Tosatti E 2011 *Nat. Commun.* **2** 236
- [7] Pruttivarasin T, Ramm M, Talukdar I, Kreuter A and Häfner H 2011 *New J. Phys.* **13** 075012
- [8] Mandelli A, Vanossi A and Tosatti E 2013 *Phys. Rev. B* **87** 195418
- [9] Fogarty T, Cormick C, Landa H, Stojanović V M, Demler E and Morigi G 2015 *Phys. Rev. Lett.* **115** 233602
- [10] Braun O M and Kivshar Y S 2013 *The Frenkel-Kontorova Model: Concepts, Methods, and Applications* (Springer Science & Business Media)
- [11] Aubry S 1983 *Physica D* **7** 240–258
- [12] Sharma S, Bergersen B and Joos B 1984 *Phys. Rev. B* **29** 6335–6340
- [13] Braiman Y, Baumgarten J, Jortner J and Klafter J 1990 *Phys. Rev. Lett.* **65** 2398
- [14] Bylinskii A, Gangloff D and Vuletić V 2015 *Science* **348** 1115–1118
- [15] Gangloff D, Bylinskii A, Counts I, Jhe W and Vuletić V 2015 *Nat. Phys.* **11** 915–919
- [16] Counts I, Gangloff D, Bylinskii A, Hur J, Islam R and Vuletić V 2017 *Phys. Rev. Lett.* **119** 043601
- [17] Bylinskii A, Gangloff D, Counts I and Vuletić V 2016 *Nat. Mater.* **15** 717–721
- [18] Matsukawa H and Fukuyama H 1994 *Phys. Rev. B* **49** 17286
- [19] Kiethe J, Nigmatullin R, Kalincev D, Schmirander T and Mehlstäubler T 2017 *Nat. Commun.* **8** 15364
- [20] Mielenz M, Brox J, Kahra S, Leschhorn G, Albert M, Schätz T, Landa H and Reznik B 2013 *Phys. Rev. Lett.* **110** 133004
- [21] Pyka K, Keller J, Partner H L, Nigmatullin R, Burgermeister T, Meier D, Kuhlmann K, Retzker A, Plenio M, Zurek W, del Campo A and Mehlstäubler T 2013 *Nat. Commun.* **4** 2291
- [22] Ulm S, Roßnagel J, Jacob G, Degünther C, Dawkins S, Poschinger U, Nigmatullin R, Retzker A, Plenio M, Schmidt-Kaler F and Singer K 2013 *Nat. Commun.* **4** 2290
- [23] Ejtemaee S and Haljan P 2013 *Phys. Rev. A* **87** 051401
- [24] Kumar S and Li M S 2010 *Phys. Rep.* **486** 1–74
- [25] Sieradzan A K, Niemi A and Peng X 2014 *Phys. Rev. E* **90** 062717
- [26] del Campo A, De Chiara G, Morigi G, Plenio M and Retzker A 2010 *Phys. Rev. Lett.* **105** 075701
- [27] Silvi P, Morigi G, Calarco T and Montangero S 2016 *Phys. Rev. Lett.* **116** 225701
- [28] De Chiara G, del Campo A, Morigi G, Plenio M B and Retzker A 2010 *New J. Phys.* **12** 115003
- [29] Landa H, Marcovitch S, Retzker A, Plenio M and Reznik B 2010 *Phys. Rev. Lett.* **104** 043004
- [30] Landa H, Retzker A, Schätz T and Reznik B 2014 *Phys. Rev. Lett.* **113** 053001
- [31] Brox J, Kiefer P, Bujak M, Schätz T and Landa H 2017 *Phys. Rev. Lett.* **119** 153602
- [32] Keller J, Burgermeister T, Kalincev D, Didier A, Kulosa A, Nordmann T, Kiethe J and Mehlstäubler T 2018 *arXiv*

- preprint arXiv:1803.08248*
- [33] Herschbach N, Pyka K, Keller J and Mehlstäubler T E 2012 *Appl. Phys. B* **107** 891–906
 - [34] Landa H, Reznik B, Brox J, Mielenz M and Schätz T 2013 *New J. Phys.* **15** 093003
 - [35] Partner H L, Nigmatullin R, Burgermeister T, Pyka K, Keller J, Retzker A, Plenio M B and Mehlstäubler T E 2013 *New J. Phys.* **15** 103013
 - [36] Nigmatullin R, del Campo A, De Chiara G, Morigi G, Plenio M B and Retzker A 2016 *Physical Review B* **93** 014106
 - [37] Partner H L, Nigmatullin R, Burgermeister T, Keller J, Pyka K, Plenio M B, Retzker A, Zurek W H, del Campo A and Mehlstäubler T E 2015 *Physica B* **460** 114–118
 - [38] Vanossi A, Röder J, Bishop A and Bortolani V 2003 *Phys. Rev. E* **67** 016605
 - [39] Pyka K, Herschbach N, Keller J and Mehlstäubler T E 2014 *Appl. Phys. B* **114** 231–241
 - [40] Skeel R D and Izaguirre J A 2002 *Mol. Phys.* **100** 3885–3891
 - [41] Gudjons T, Seibert P and Werth G 1997 *Appl. Phys. B* **65** 57–62
 - [42] Landa H, Drewsen M, Reznik B and Retzker A 2012 *New J. Phys.* **14** 093023
 - [43] Ghosh P 1995 *Ion traps* (Oxford: Clarendon Press)
 - [44] Keller J, Kalincev D, Burgermeister T, Kulosa A, Didier A, Nordmann T, Kiethe J and Mehlstäubler T 2017 *arXiv preprint arXiv:1712.02335*
 - [45] Kaufmann H, Ulm S, Jacob G, Poschinger U, Landa H, Retzker A, Plenio M and Schmidt-Kaler F 2012 *Phys. Rev. Lett.* **109** 263003
 - [46] Ibaraki Y, Tanaka U and Urabe S 2011 *Appl. Phys. B* **105** 219–223
 - [47] Morigi G, Eschner J and Keitel C H 2000 *Phys. Rev. Lett.* **85** 4458
 - [48] Lechner R, Maier C, Hempel C, Jurcevic P, Lanyon B P, Monz T, Brownnutt M, Blatt R and Roos C F 2016 *Phys. Rev. A* **93** 053401
 - [49] Scharnhorst N, Cerrillo J, Kramer J, Leroux I D, Wübbena J B, Retzker A and Schmidt P O 2017 *arXiv preprint arXiv:1711.00738*
 - [50] Ejtemaee S and Haljan P 2017 *Phys. Rev. Lett.* **119** 043001
 - [51] Zanca T, Pellegrini F, Santoro G E and Tosatti E 2018 *Proc. Natl. Acad. Sci.* **115** 3547–3550
 - [52] Li H K, Urban E, Noel C, Chuang A, Xia Y, Ransford A, Hemmerling B, Wang Y, Li T, Häfner H and Zhang X 2017 *Phys. Rev. Lett.* **118** 053001

Appendix

Offset of the primary gap in the hull function

In Figure 3(c) for $\alpha = 6.6$, the central gap is offset from $z_{j,0} = 0$ and $z_j = 0$. This is due to broken mirror symmetry of the system. The topological defect is already in one of the central PN potential wells, see Figure 2(c). The defect is not situated at the position of the PN barrier, and neither are the ions, for which we calculate the hull function. Before a slip can occur, the ions first need to move in either axial direction, which is the reason why the primary gap is not at $z_{j,0} = 0$. Due to the inhomogeneity the localized defect moves towards one central minimum (towards the right in the figures), instead of the other, were the PN potential becomes steeper. This explains why the gap is not symmetric around $z_j = 0$.

Simulation Overview

Throughout this paper we used different numerical calculations depending on the issue at hand. The following list and Table 1 gives a short description of each method and where it was used.

- two-dimensional calculation using time-averaged rf potentials without temperature. This code solves the equations of motion of all ions in the ponderomotive approximation of the rf field under high damping to get the equilibrium positions $\mathbf{q}(0)$. $T = 0\text{K}$. It also allows for the diagonalization of Hessian matrix for a given $\mathbf{q}(0)$, resulting in the mode spectrum of the crystal, and the calculation of the hull functions.
- three-dimensional calculation using time-averaged rf potentials with temperature. This code solves the Langevin equations for all ions in the ponderomotive approximation for the rf field in three dimensions under experimentally realistic damping. The temperature is introduced with a stochastic force. Vibrational mode frequencies are obtained with Fourier transformation of the resulting ion trajectories.
- three-dimensional calculation of time-dependent rf potentials without temperature. This code solves the Mathieu equations [43] for all ions in three dimensions under damping. The average positions of the ions are taken as the equilibrium positions for comparison with the ponderomotive approximation.

Dimensions	EOM solved for	Temperature	Used in Figures
2	time-averaged rf potential	0 K	2(b), 3(b), 5(b), 7, 9, 10, 12
3	time-averaged rf potential	> 0 K	5(b), 6
3	time-dependent rf potential	0 K	8

Table 1. Overview showing in which Figure each type of numerical calculation is used. EOM: equations of motion